

A Stochastic Model for Wind-Driven Currents Over the Continental Shelf

K. H. BRINK AND D. C. CHAPMAN

Woods Hole Oceanographic Institution, Woods Hole, Massachusetts

G. R. HALLIWELL, JR.¹

College of Oceanography, Oregon State University, Corvallis

A stochastic model for current, pressure, and density fluctuations over the continental shelf and slope is solved for coherence, phase, and gain between the oceanographic variables and wind stress. Comparison of wind stress spectra and transfer functions show that free coastal-trapped wave physics tends to exist in a frequency band bounded at the low end because of frictional predominance and at the high end because of the absence of wind energy at appropriate alongshore length scales. The transfer functions for density and especially cross-shelf velocity show that these variables are sensitive to short length scales in the forcing and are thus difficult to predict in general. Model results are compared to observations of bottom pressure and alongshore velocity from the 1982 Coastal Ocean Dynamics Experiment off northern California. The results agree with observations, at least qualitatively, with regard to spatial and frequency patterns in coherence and gain. The poorest point of agreement is in the amplitude of wind stress-current gains, which the model systematically underpredicts. The comparisons do demonstrate the importance of including accurate representations of bottom friction and of both cross-shelf and alongshore gradients of wind stress amplitude.

1. INTRODUCTION

Over the past decade, considerable effort has gone into long-wave models of fluctuating currents over the continental shelf and slope. Such models normally involve solving a set of first-order wave equations, using observed winds as inputs, while seeking to hindcast observed current fluctuations. The approach, which is often at least qualitatively successful [e.g., *Battisti and Hickey*, 1984; *Mitchum and Clarke*, 1986a], generally involves several simplifying assumptions and is cast rather rigidly in terms of the free long coastal-trapped wave modal structures.

An alternative approach to evaluating the potential skill of linearized shelf models is presented here. The present study relaxes the "long-wave" assumption made, for example, by *Clarke and Brink* [1985] and does not use the first-order wave equation formalism. Instead, we use a linear model to hindcast statistical properties of the shelf-slope flow field and to compare these statistics with observations. This stochastic approach was first applied to shelf models by *Spillane* [1980] for a barotropic case which resolved frictional boundary layers. Also, a problem analogous to ours was done for the deep ocean by *Müller and Frankignoul* [1981]. While this approach is nominally independent of the first-order wave equation theories, it will become clear that there are numerous interconnections. In this regard, the illuminating study of *Allen and Denbo* [1984] can be seen to anticipate some of our results. One advantage of the stochastic approach is that the variations in results due to changes in particular model inputs (e.g., stratification or friction) can be isolated in a straightforward way.

The following study is centered about the Coastal Ocean Dynamics Experiment (CODE) observations made off north-

ern California in 1982. This data set provides an unusually good resolution of both model inputs and of the predicted fields. The reader is referred to *Winant et al.* [this issue] for an introduction to the results of the program.

The remaining sections are organized as follows. First, the model is formulated, and its implementation is explained. Next, a physical discussion of the model's attributes is given, followed by a presentation of model outputs and their parameter sensitivity. Then observational results are presented and compared to a "best estimate" model. Finally, conclusions are drawn.

2. FORMULATION

The modeling approach is to compute theoretical transfer functions between wind stress and observable quantities in the frequency and alongshore wave number domain. The transfer functions are then integrated over wave number space, using observed wind wave number spectra, to estimate observable statistics in the frequency domain. This approach requires that the model be uniform in the alongshore direction in that the Coriolis parameter f , stratification, and shelf topography can not vary. This precludes, for example, potentially important processes such as topographically induced coastal-trapped wave scattering.

The geometry is shown in Figure 1. The model coast lies at $x = 0$, and the coastal barrier is placed where the estimated Ekman scale depth is one third of the water depth, consistent with the long-wave results of *Mitchum and Clarke* [1986b]. The system rotates at a uniform rate of $f/2$, and linearized, Boussinesq dynamics apply throughout. Attention is limited to cases with frequencies less than the inertial. Dissipative and mixing processes occur only in infinitesimally thin surface and bottom boundary layers. The thin boundary layer approximation is reasonable if the vertical scales of the interior solution are large in relation to the true boundary layer thickness (e.g., 10 m). Thus the effect of these diabatic regions will appear only through the boundary conditions. Under these assumptions, the equations governing flow outside the bound-

¹ Now at Graduate School of Oceanography, University of Rhode Island, Narragansett.

Copyright 1987 by the American Geophysical Union.

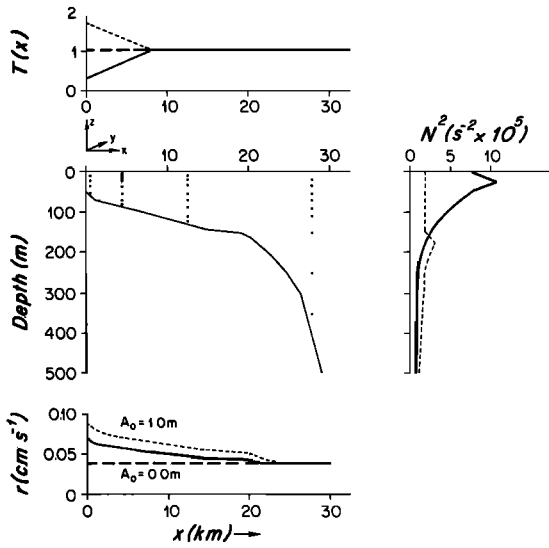


Fig. 1. Schematic of model geometry, showing various parameter values. (top) Strength of wind stress as a function of cross-shelf distance. The solid line corresponds to the basic case study. (middle) Actual CODE central line topography. Dots indicate positions of current meters. (right) Brunt-Väisälä frequency squared, N^2 . The solid line is the basic case. (bottom): Bottom resistance coefficient r as a function of cross-shelf position. The solid line is the basic case, $A_0 = 0.5$ m. The mooring locations are C2, $x = 2$ km; C3, $x = 5.8$ km; C4, $x = 12.5$ km; and C5, $x = 27.3$ km.

ary layers are

$$u_t - fv = -\frac{1}{\rho_0} p_x \tag{1a}$$

$$v_t + fu = -\frac{1}{\rho_0} p_y \tag{1b}$$

$$0 = -p_z - g\rho' \tag{1c}$$

$$u_x + v_y + w_z = 0 \tag{1d}$$

$$\rho'_t + w\bar{\rho}_z = 0 \tag{1e}$$

where u , v , and w are the onshore, alongshore, and vertical velocities, respectively, and p is the pressure perturbation. The density field is broken up as

$$\rho = \rho_0 + \bar{\rho}(z) + \rho'(x, y, z, t)$$

(where ρ' is small in relation to $\bar{\rho}$, and $\bar{\rho}$ is small in relation to ρ_0). Subscripts x , y , z , and t represent partial derivatives with respect to the onshore, alongshore, and vertical coordinates and to time, respectively. The Coriolis parameter and acceleration due to gravity are given respectively by f and g .

The boundary conditions are

$$0 = \left(f^2 + \frac{\partial^2}{\partial t^2}\right)(w + h_x u) - (frv_B + ru_{Bt})_x - r(v_t - fu)_y \tag{2a}$$

$$z = -h(x)$$

$$0 = \left(f^2 + \frac{\partial^2}{\partial t^2}\right)(-\rho_0 w + g^{-1} p_t) + (\tau_{0t}^x + f\tau_{0t}^y)_x + (-f\tau_{0t}^x + \tau_{0t}^y)_y \quad z = 0 \tag{2b}$$

$$0 = -(f\bar{p}_y + p_{xt})h + f(\tau_{0t}^y - \rho_0 r v) + (\tau_{0t}^x - \rho_0 r u)_t \tag{2c}$$

$$x = 0$$

$$0 = u_x \quad x = L \tag{2d}$$

The wind stress vector is (τ_0^x, τ_0^y) , and the water depth is $h(x)$. Subscript B means that the variable is evaluated at the bottom before partial differentiation. Conditions (2a)–(2c) are derived in manners analogous to those presented by *Clarke and Brink* [1985]. The bottom resistance coefficient r occurs because of the assumed bottom stress form

$$\tau_B = \rho_0 r \mathbf{v} \tag{3}$$

where \mathbf{v} is evaluated at the bottom. The value of r takes into account the gravity wave effect discussed by *Grant and Madsen* [1979] and is linearized using typical observed near-bottom velocities and the averaging procedure of *Wright and Thompson* [1983]. The resulting values are shown in Figure 1. The bottom boundary condition (2a) reflects Ekman pumping and the condition of no flow through the true bottom. The surface boundary condition (2b) represents a “free surface” and the effect of Ekman pumping. A rigid lid could be imposed by deleting the term $g^{-1} p_t$ in (2b). The “coastal” boundary condition (2c) expresses the constraint that there is no net flow through this wall. Finally, condition (2d) is imposed at some large but finite distance L offshore where the bottom is flat, and is simply a form that is believed to be a reasonable approximation to the true boundedness condition [see *Brink*, 1982].

The solution approach to the above system will be to assume that the wind stress has the form

$$\tau_0^y = T^y(x) \exp [i(\omega t + ly)]$$

or

$$\tau_0^x = T^x(x) \exp (i(\omega t + ly)) \tag{4a}$$

where l is complex:

$$l = l_R + il_I \tag{4b}$$

and T^x and T^y are constant far from shore. Assuming that all other variables also have the harmonic form allows the derivation of a single equation for the pressure transfer function $\bar{p}(x, l, z, \omega)$ in the frequency–alongshore wave number domain:

$$\bar{p}_{xx} - l^2 \bar{p} + (f^2 - \omega^2) \left(\frac{\bar{p}_z}{N^2}\right)_z = 0 \tag{5}$$

where $N^2 (= -g\rho_0^{-1} \bar{\rho}_z)$ is the Brunt-Väisälä frequency squared. This equation is then to be satisfied subject to conditions (2) in their harmonic forms. It is straightforward to solve (5) numerically on a stretched 25 by 17 grid using a program documented by *Brink and Chapman* [1985]. The pressure transfer function \bar{p} is the basis of the calculations presented by *Clarke and Brink* [1985], although they made some additional simplifying assumptions.

Results which depend upon alongshore wave number, such as $\bar{p}(x, l, z, \omega)$, are difficult to compare with observations. Thus it is desirable to express model results as a function of position and frequency. The bridge between theory and observation comes through integrating model results across the real wave number space

$$\hat{S}_{pT}(x, z, \omega) = \int_{-\infty}^{\infty} \bar{p}(x, l, z, \omega) S_T(l_R, \omega) dl_R \tag{6}$$

where S_T is the observed alongshore wave number–frequency spectrum of the wind stress and \hat{S}_{pT} then is the predicted cross spectrum of wind stress and pressure. Further, the model

autospectrum of pressure is given by

$$\hat{S}_p(x, z, \omega) = \int_{-\infty}^{\infty} |\bar{p}(x, l, z, \omega)|^2 S_T(l_R, \omega) dl_R \quad (7)$$

The frequency domain (only) wind stress spectrum is given by

$$\hat{S}_T(\omega) = \int_{-\infty}^{\infty} S_T(l_R, \omega) dl_R \quad (8)$$

This allows the calculation of model wind-pressure coherence

$$\gamma_{pT} = |\hat{S}_{pT}(x, z, \omega)| [\hat{S}_p(x, z, \omega) \hat{S}_T(\omega)]^{-1/2} \quad (9a)$$

and phase

$$\theta_{pT}(x, z, \omega) = \arg [\hat{S}_{pT}(x, z, \omega)] \quad (9b)$$

Similar expressions for other variables can be obtained by deriving their transfer function in terms of pressure, e.g.,

$$\bar{u}(x, l, z, \omega) = \rho_0^{-1} (f \bar{p}_x + \omega l \bar{p}) (f^2 - \omega^2)^{-1}$$

and then proceeding by analog to (6)–(9). In the following, model results and observations will be compared in terms of grain

$$\begin{aligned} R_{pT}(x, z, \omega) &= \hat{S}_T^{-1} \left| \int_{-\infty}^{\infty} \bar{p} S_T dl_R \right| = \hat{S}_T^{-1} \hat{S}_{pT} \\ &= \gamma_{pT} (\hat{S}_p / \hat{S}_T)^{1/2} \end{aligned}$$

coherence, and phase. Other groupings of results (e.g., cross spectrum and pressure autospectrum) would give comparable results, but the present choice is preferable because it does not depend explicitly on the absolute amplitude of the observed wind spectrum (although it does, of course, depend considerably on the shape of the observed wind spectrum).

3. WIND STRESS SPECTRUM AND INTEGRATION

The space-time spectrum of the alongshore wind stress has been estimated using *Bakun* [1973] wind stress estimates, as described by G. R. Halliwell and J. S. Allen (Seasonal differences in the response of coastal sea level to alongshore wind stress along the west coast of North America, 1980–1984, analyzed in wave number–frequency space, submitted to *Journal of Geophysical Research*, 1986). These stress estimates are derived from geostrophic winds and have a simple boundary layer correction (uniform reduction and veering) applied. The winds were then individually rotated further to improve their correlation with measured winds. Details of this procedure can be found in the paper by *Halliwell and Allen* [this issue]. These wind stress records were available at 6-hour intervals at alongshore separations of 180 km. From these data it was then straightforward to estimate the spectrum with a resolution of $\Delta l = 2.5 \times 10^{-8} \text{ cm}^{-1}$ and $\Delta \omega = 3.0 \times 10^{-6} \text{ s}^{-1}$. The Bakun spectrum for summer 1982 is shown in Figure 2a. The data, by their nature, are effectively low-pass filtered in time, so they cannot be considered reliable for frequencies greater than around $3.55 \times 10^{-5} \text{ s}^{-1}$ (0.5 cpd). Likewise, there is considerable spatial smoothing involved in these stress estimates. It appears that the absence of information on scales less than at least 180–360 km leads to a substantial underestimate of energy at short wavelengths [*Halliwell and Allen*, this issue]. As will be discussed below, this may not be a serious problem for predicting pressure and alongshore currents.

The cross spectrum between wind stress at locations sepa-

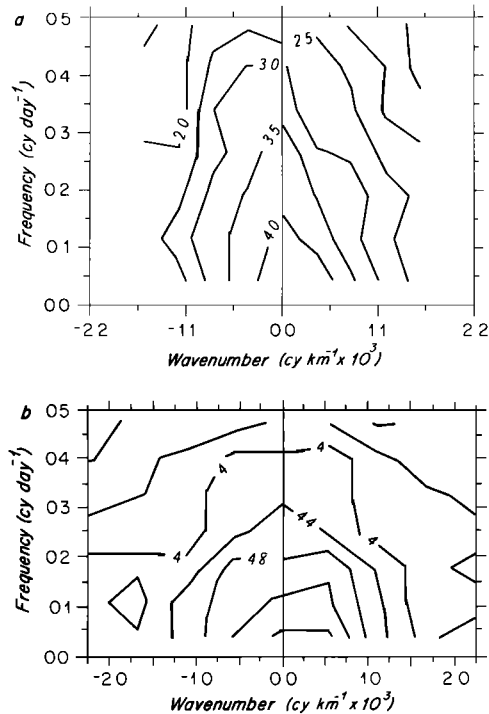


Fig. 2. (a) Frequency–alongshore wave number spectrum of alongshore wind stress, derived from Bakun winds. Units are the base 10 log of $(\text{dyn cm}^{-2}) (\text{cpkm})^{-1} (\text{cpd})^{-1}$. (b) Same as Figure 2a except for the measured wind stress spectrum.

rated by a distance Δy is

$$\hat{S}_{TT}(\Delta y, \omega) = \int_{-\infty}^{\infty} S_T(l_R, \omega) e^{i l_R \Delta y} dl_R \quad (10a)$$

and the coherence is

$$\gamma_{TT}(\Delta y, \omega) = S_T(\omega)^{-1} |\hat{S}_{TT}| \quad (10b)$$

This “calculated” coherence estimate, based on Bakun wind results, has been compared to the coherence between measured wind stresses at National Data Buoy Office NDBO buoys 46013 (38°N) and 46011 (35°N), with $\Delta y = 455 \text{ km}$. The integrals over wave number in all cases which follow are computed by trapezoidal rule, with 21 values of S_T available at each frequency, corresponding to $|l_R|$ of less than $1.25 \times 10^{-6} \text{ cm}^{-1}$, or wavelengths longer than 500 km. At all frequencies, “calculated” coherences are extremely high (in the range of 0.95 to 0.99) in relation to coherences between measured wind stresses (in the range of 0.24 to 0.71). Even using a white wave number spectrum in (10a) over the same wave number range yields a coherence of 0.85, when it should approach zero in principle. Thus part of the discrepancy between measured and calculated coherences is simply that a broad enough wave number range of spectral estimates to make such a calculation possible is not available. A second problem is apparently that the Bakun spectral estimates are too “red”: apparently the estimates are missing energy at the higher wave numbers. This second possibility is hard to evaluate given the finite wave number range available. We therefore assume that the available wave number spectrum is accurate out to wavelengths of about 900 km [*Halliwell and Allen*, this issue]. No attempts were made to correct the spectrum for shorter wavelengths.

A second estimate of the wind stress spectrum was obtained using “measured” wind stresses (Figure 2b). This estimate is

based on a mixture of coastal and buoy wind records, and hence may reflect undesired variations in wind amplitude which are associated with distance from the coast. The measured and Bakun wind spectra are compared in detail by *Halliwel and Allen* [this issue], so we will only comment that the measured wind spectrum is considerably whiter than the Bakun spectrum as a function of wave number, particularly at higher frequencies. Since both estimates of the wind spectrum have their drawbacks (i.e., the Bakun is spatially filtered, and the measured uses uncertain amplitudes), we can not conclude which wave number distribution is more nearly correct. We should note, however, that *Chapman* [this issue] has shown that the measured winds yield much better results in first-order wave equation integrations. Thus we will use both spectra in the following, although the Bakun spectrum is used exclusively in section 4 and primarily in section 5. In section 7 the measured wind stress spectrum is used.

The cross-shelf structure of the winds is taken to have the form

$$T^y(x) = a + bx \quad L_w > x > 0 \quad (11a)$$

$$T^y(x) = c \quad x > L_w \quad (11b)$$

that is, the winds are constant beyond a distance L_w (about 8 km) from the model coastal wall. This wind structure is a rough fit to CODE observations [*Beardsley et al.*, this issue], although in practice, a and b probably vary considerably in the alongshore direction [*Halliwel and Allen*, this issue]. The spectra described above are taken to describe $c(\omega, l_R)$, and all comparisons with data will involve a wind record taken far enough from shore to be consistent. In addition, the wind stress amplitude (spectral level) is allowed to vary in the alongshore direction through the use of l_r (equation (4b)). This is a way of mimicking the observed tendency for wind fluctuations to become larger toward the north in the region between points Arguello and Reyes [e.g., *Denbo and Allen*, this issue]. Actual values were estimated by comparing spectral levels from buoys NDBO 46013 and NDBO 46011. The use of l_r can be thought of as a means to account for the spatial nonstationarity of wind stress spectra.

4. THEORETICAL TRANSFER FUNCTIONS

The following discussion is meant to relate the formalism of the stochastic theory to intuitive physical reality. Much of the insight that can be derived from the present modeling approach derives from studying the relationship between the frequency-wave number transfer functions and the wind stress spectrum. This follows from the form of the frequency domain autospectrum (equation (7)), which couples the two quantities. For example, peaks in the amplitude of \bar{v} will make little contribution to \hat{S}_p if S_T is small, and vice versa. Further, inspection of the cross spectrum (equation (6)) shows that if the phase of the transfer function varies greatly, then contributions to the integral at different l_R tend to cancel, leading to a small \hat{S}_{pT} . This in turn means that there will be little coherence (equation (9a)) with the wind, even though spectral values are high.

In the following discussion, all calculations are made using the bottom topography of the CODE central line, stratification representative of the region offshore of the shelf break, and a bottom resistance parameter estimated using *Grant and Madsen's* [1979] approach for a 15-s period incoming swell with amplitude $A_0 = 0.5$ m. Their model is linearized about a

representative near-bottom speed of 22 cm s^{-1} , derived using *Wright and Thompson* [1983], and statistics from *Limeburner* [1985]. These parameters, along with the wind stress profile $T(x)$ are illustrated by solid lines in Figure 1. Variations in these, and other, model inputs are discussed in the following section. In all cases, the Coriolis parameter is $f = 9.09 \times 10^{-5} \text{ s}^{-1}$, and the model domain extends to abyssal depths (3750 m) and to 150 km from shore. Below 500 m the N^2 profile decays with an e -folding scale of 1.5 km. Only the shelf and upper slope results, where data are available for comparison, are presented.

The transfer function and phase between wind stress and midshelf ($x = 6.25 \text{ km}$, $z = -35 \text{ m}$) alongshore velocity \bar{v} are shown in Figure 3 as a function of frequency and wave number. These values are computed assuming the wind stress magnitude is uniform all along the coast ($l_l = 0$). Distinct ridges in the magnitude of \bar{v} occur corresponding to resonance with the first and second free coastal-trapped wave modes, which have long-wave phase speeds of 299 and 153 cm s^{-1} , respectively. The ridges, like the dispersion curves, show little curvature over the frequency wave number range. Higher-mode resonances are generally weaker. In the vicinity of the response maxima, wind-current phase also changes rapidly, a characteristic which leads to low wind-current coherence if the resonant response dominates (equation (7)). Physically, this can be taken to mean that much of the alongshore velocity variance is due to coastal-trapped waves generated by winds far to the south, and those winds are incoherent with the local winds. This dominance of remote forcing manifests itself through low coherence between local winds and currents.

The wind-current coupling as a function of frequency can be examined by comparing the Bakun wind spectrum and the transfer function (Figure 4). The wind energy is highest at the largest scales (near $l_R = 0$), so that strongest responses are obtained when the transfer function is large at small wave numbers. Thus at low frequency ($\omega = 0.38 \times 10^{-5} \text{ s}^{-1}$), a large velocity response (spectrum) should be found after integration over wavenumber, although low coherence may be

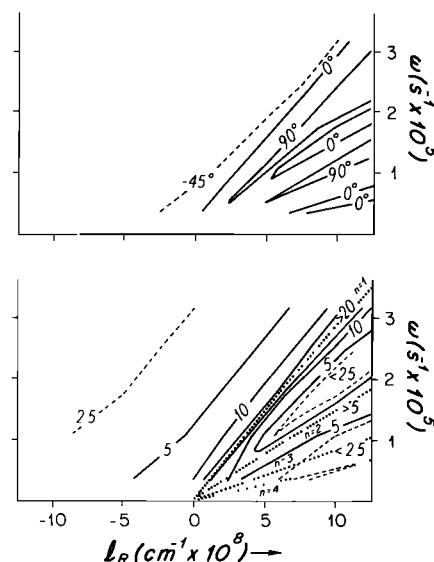


Fig. 3. Transfer function \bar{v} as a function of frequency and real alongshore wave number for $l_l = 0.0$. The position is $x = 6.25$, $z = -35 \text{ m}$. (top) Phase. (bottom) Amplitude in $\text{cm s}^{-1} (\text{dyn cm}^{-2})^{-1}$. The first four coastal-trapped wave modes' dispersion curves are shown by heavy dotted lines.

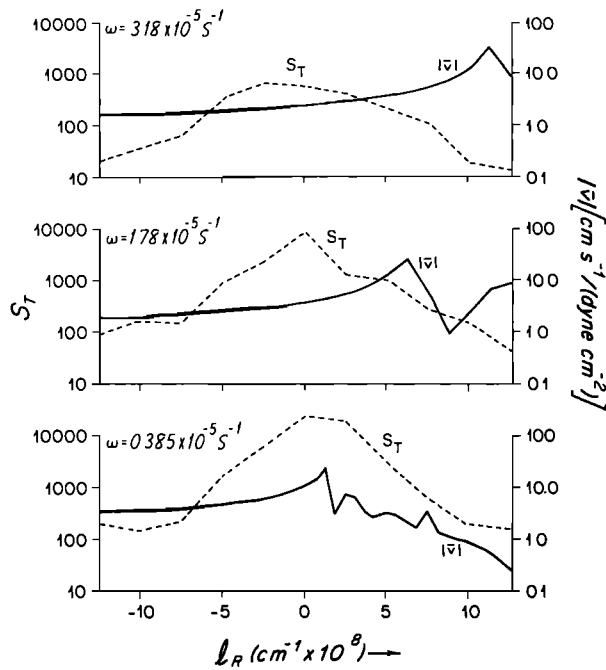


Fig. 4 Wind stress spectrum S_T and alongshore velocity transfer function amplitude $|\bar{v}|$ (evaluated at $x = 6.25$ km, $z = -35$ m) as a function of alongshore wave number for $l_I = 0$. The units of S_T are $(\text{dyn cm}^{-2})^2 (\text{cpkm}^{-2})^{-1} (\text{cpd})^{-1}$. Note the logarithmic scale.

expected, due to near-resonant phase shifts. This tendency for low coherence at low frequency is mitigated, however, because frictional effects at $\omega = 0.38 \times 10^{-5} \text{ s}^{-1}$ are large enough to lessen near-resonant phase shifts (Figure 3). At slightly higher frequencies ($\omega = 1.08 \times 10^{-5} \text{ s}^{-1}$ or $\omega = 1.78 \times 10^{-5} \text{ s}^{-1}$), the phase shifts are much more pronounced, and lower coherence is to be expected. At high frequencies ($\omega = 3.18 \times 10^{-5} \text{ s}^{-1}$), the peak in spectral transfer function occurs at high wave number, far from the peak in Bakun wind energy. In this case the response (spectrum) of current should be weaker but much more coherent because of the relatively uniform phase of the transfer function away from resonance. The increase in coherence at high frequency will be less pronounced if the wave number spectrum of the true wind is less sharply peaked than that for the Bakun winds. This is the case with the measured wind stress spectrum. In summary, the energy of currents should decrease as frequency increases because of the decreasing trend in wind spectral density and because of the growing mismatch in the locations of wind and transfer function peaks as a function of l_R . Wind-current coherence should initially decrease with frequency because of the lessening of frictional influences, which are roughly proportional to $r(\omega h)^{-1}$ [Clarke and Brink, 1985]. At high frequencies, coherence should tend to increase because of the decreasing importance of free wave resonance. Further, the first-mode resonance will generally dominate the second-mode resonance, both because of the shape of the wind spectrum (it is always larger at the smaller l_R corresponding to the first mode) and because of damping effects evident in \bar{v} as a function of l_R (i.e., the second-mode ridge in Figure 3 is less pronounced than the first-mode ridge).

The above comments about alongshore velocity response apply in a similar manner to the pressure response. The only substantial difference is that the pressure transfer function (Figures 5 and 6) shows a secondary ridge near $l_R = 0$ corresponding to resonance with the barotropic Kelvin wave (phase

speed of $18,700 \text{ cm s}^{-1}$). This wave mode does not show up in any of the other variables because of its large cross-shelf scale. Both pressure and alongshore velocity have transfer functions which decrease fairly quickly for large magnitudes of l_R (except near resonance), so that prediction of these variables will depend mainly on estimating only the small-wave number (large scale) portion of the wind spectrum correctly. If one thinks of this in terms of the first-order wave equation governing long coastal-trapped waves [e.g., Gill and Schumann, 1974], this makes sense: the integral form of their solution smooths out small-scale wind fluctuations, at least at low frequencies. Thus the success of long coastal-trapped wave theory for estimating pressures or alongshore currents [e.g., Battisti and Hickey, 1984; Mitchum and Clarke, 1986a] can be reconciled with the stochastic formulation.

The two other variables of interest, cross-shelf velocity u and density ρ , present a rather different picture (Figure 6; note the scale differences). The results are presented at $\omega = 1.08 \times 10^{-5} \text{ s}^{-1}$. The density transfer function does not vary as much with wave number (at least at $x = 6.25$ km, $z = -35$ km), and the nonresonant response (large negative l_R) is almost as large as that for the first-mode resonance. Phase (not shown) also does not vary as radically as for alongshore velocity. Cross-shelf velocity has an even more interesting behavior: it increases nearly linearly with increasing negative l_R out to a maximum of about $2 \text{ cm s}^{-1} (\text{dyne cm}^{-2})^{-1}$ at $l_R = -1.0 \times 10^{-6} \text{ cm}^{-1}$. Thus the peak nonresonant response is greater than the first-mode resonant response. Because these transfer functions do not fall off as quickly as those for v or p , density and, especially, cross-shelf velocity will be very dependent on the smallest scales in the wind stress field. This, in turn, suggests that predictability of cross-shelf velocity will depend critically on the estimation of wind stress variability at scales so small as often to be impractical to measure. This lack of predictability of u , therefore, does not depend upon alongshore variations in topography (an effect omitted from this model), which will further complicate predictability of onshore flow [e.g., Brink, 1980]. Results at other frequencies lead to similar conclusions. In summary, the broad distribution of u and ρ transfer functions versus wave number implies a considerable dependence on the poorly resolved small-scale part of the wind spectrum. Indeed, calculations of the sort presented below provide very poor representations of these variables.

All of the above discussion has centered on the case of uniform wind magnitudes all along the coast ($l_I = 0$). Exploring the response as a function of complex wave number is also enlightening and relevant because of the known alongshore variability in wind stress amplitude along the U.S. west coast

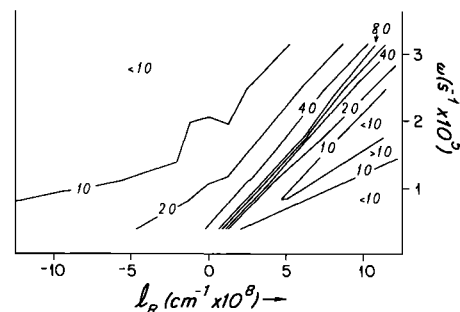


Fig. 5. Amplitude of "coastal" pressure response $|\bar{p}|$ (evaluated at $x = 0.0$ km, $z = 0.0$ m) as a function of frequency and alongshore wave number for $l_I = 0.0$. Units are $\text{mbar} (\text{dyn cm}^{-2})^{-1}$.

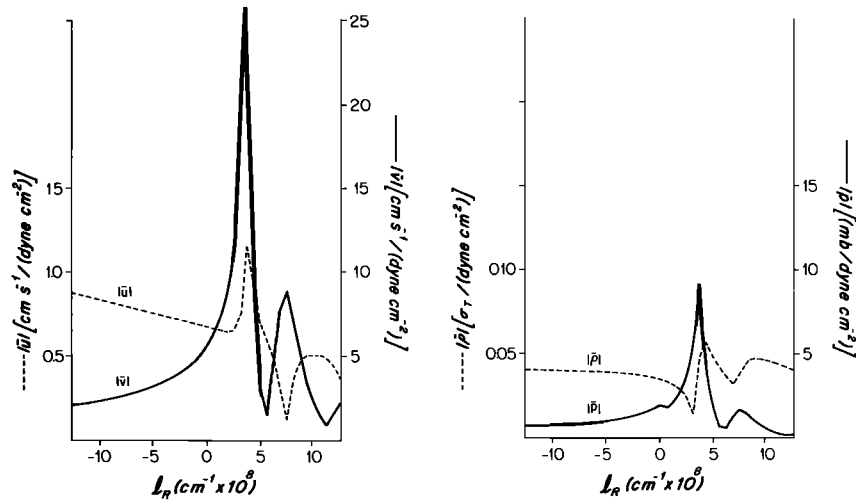


Fig. 6. Amplitudes of transfer functions as a function of wave number for $l_1 = 0.0$ and $\omega = 1.08 \times 10^{-5} \text{ s}^{-1}$. Both velocity components and $|p|$ are evaluated at $x = 6.25 \text{ km}$ and $z = -35 \text{ m}$, and $|p_T|$ is evaluated at $x = 0.0 \text{ km}$, $z = 0.0 \text{ m}$.

[e.g., Denbo and Allen, this issue]. The transfer function of alongshore velocity at $x = 6.25 \text{ km}$, $z = -35 \text{ m}$ at the single frequency $\omega = 1.08 \times 10^{-5} \text{ s}^{-1}$ is shown as a function of complex wave number in Figure 7. For $l_1 < 0$, the amplitude of the forcing decreases toward $-y$ (i.e., toward the north on the west coast of the United States), and two maxima exist, corresponding to complex near-resonances with the first two coastal-trapped wave modes. These complex “resonances” are associated with the frictional decay of the waves as they propagate northward; i.e., the free, frictional waves and the wind magnitudes vary in the same sense. Physically, these response maxima would lead to strong, nonlocally driven currents because the local wind driving would be overshadowed by stronger, less coherent, forcing to the south. The upper half-plane ($l_1 > 0$) corresponds to motions which grow stronger to the north (on the west coast) and contains no resonant peaks. Phase changes as a function of wave number are much less pronounced than for $l_1 < 0$, meaning that currents would tend to be more coherent with local winds. Physically, this situation corresponds to winds southward of the observation point which are too weak to generate propagating disturbances of sufficient magnitude to mask the local contribution to driving.

The above discussion rationalizes some observed phenomena such as variations of wind-current coherence versus frequency and versus the north-south trend in wind fluctuation amplitude. Perhaps the most striking result is the dependency of the cross-shelf velocity component on the shorter scales in the wind field, which in turn may explain the observed short spatial scales of this variable.

5. MODEL COHERENCE, PHASE, AND TRANSFER FUNCTION SENSITIVITY

Once the frequency-wave number transfer functions have been computed, it is straightforward to compute integrals of the type of (6), (7), and (8) numerically. The results are frequency- and position-dependent quantities which can be readily compared to observables. Specifically, all comparisons are based on coherence γ , phase θ , and gain R . First, results from one example are discussed in detail, and then variations due to changes in particular model inputs are considered.

Unless noted otherwise, all calculations in this section were done using the Bakun wind stress spectrum (Figure 2a).

5.1. A Basic Example

A first example is to consider the parameters given in the preceding section and displayed in Figure 1: $A_0 = 0.5 \text{ m}$, $l_1 = 0.0$, $L_w = 8 \text{ km}$, and deep-sea stratification. The parameter choice represents a rough approximation of conditions off northern California during spring and summer 1982. Results as a function of x and z are shown only for $\omega = 1.08 \times 10^{-5} \text{ s}^{-1}$ (6.7-day period), a frequency typical of wind-driven current fluctuations.

The alongshore velocity component (Figure 8, top panels) is used as a basis for comparison in the following sensitivity studies. The model coherence of currents with local wind is highest near the surface at midshelf and falls off with depth and distance offshore. Phase lags are such that nearshore and deeper motions generally lead those farther offshore in time, a feature often associated with frictional effects [e.g., Brink and Allen, 1983]. This trend reverses at depth over the slope, where coherence and gain become small. The gain R_{vT} has the same general shape as coherence, peaking at around $6 \text{ cm s}^{-1} (\text{dyn cm}^{-2})^{-1}$ at midshelf near the surface.

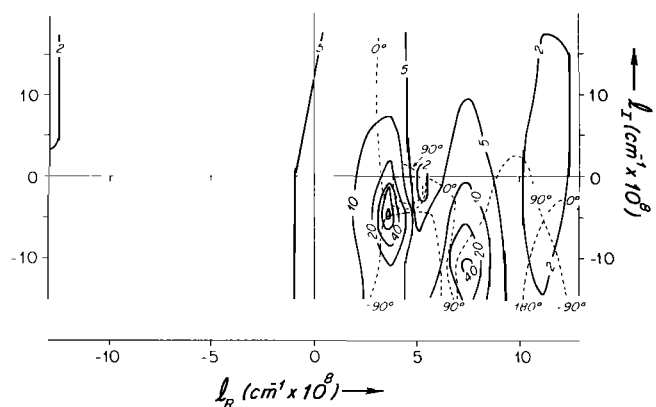


Fig. 7. Transfer function for alongshore velocity $|v|$ (evaluated at $x = 6.25 \text{ km}$, $z = -35 \text{ m}$) as a function of complex wave number for $\omega = 1.08 \times 10^{-5} \text{ s}^{-1}$. Solid contours are amplitude in $\text{cm s}^{-1} (\text{dyn cm}^{-2})^{-1}$, and dashed lines are the phase.

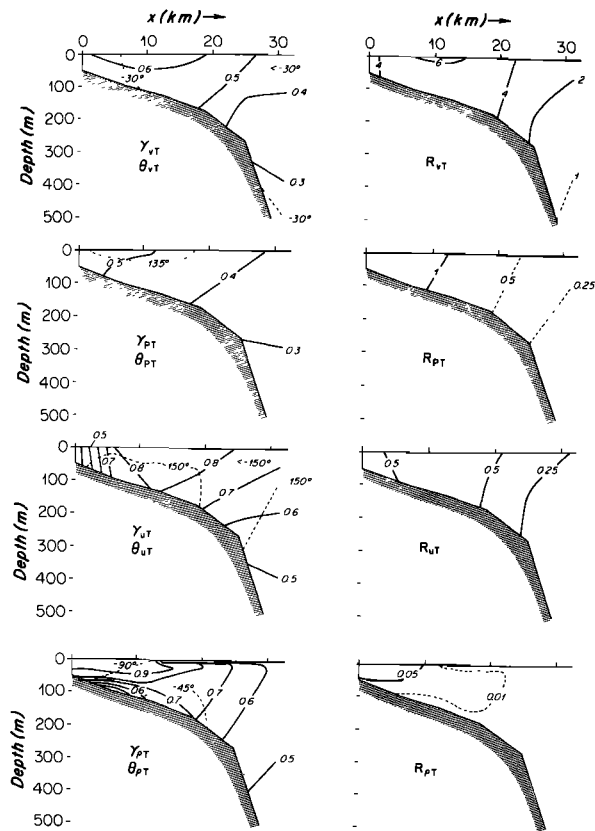


Fig. 8. Basic case model results for $\omega = 1.08 \times 10^{-5} \text{ s}^{-1}$. The top row is for alongshore velocity v , the second is for pressure p , the third is for cross-shelf velocity u , and the last is for density ρ . Left panels are wind-current coherence γ (solid contours) and phase θ (dotted contours). Right panels are gains. Units for R_{vT} and R_{uT} are $\text{cm s}^{-1} (\text{dyn cm}^{-2})^{-1}$, those for R_{pT} are $\text{mbar} (\text{dyn cm}^{-2})^{-1}$, and those for $R_{\rho T}$ are $\sigma_t (\text{dyn cm}^{-2})^{-1}$. Dashed lines for gain are used for contours representing increments less than those on the rest of the plot.

Some feel for the frequency dependence of model response can be obtained from plots of alongshore velocity behavior at 50-m depth versus distance offshore and frequency (Figure 9). The coherence is always a maximum at midshelf ($x = 6\text{--}10$ km) and has a minimum at about $1.08 \times 10^{-5} \text{ s}^{-1}$. Phases increase monotonically with frequency at all positions, and the maximum lag always occurs over the middle to outer shelf ($x = 10\text{--}15$ km). In the inner 10 km only, motions closer to shore always lead those farther offshore. This gradient is most interesting at the lowest frequency, where currents close to the coast actually lead the wind. The gain R_{vT} (Figure 9) is always a maximum at midshelf, and it decreases monotonically with increasing frequency. It should also be noted that many of the characteristics (such as midshelf gain maximum and phase minimum) of the R_{vT} and θ_{vT} plots occur in the individual wave number-domain transfer functions \bar{v} and are not a result of the spectral summations.

Results for pressure versus wind stress statistics (Figure 8, second row) are broadly similar to those for alongshore velocity, with a few exceptions. First, the coherence and gain are a maximum near the "coastal" wall, rather than at midshelf. Second, wind-pressure coherence is typically about 0.1 lower than for velocity over the shelf, although for observations, the opposite is true. Finally, cross-shelf and vertical phase differences tend to be less than for velocity. The tendencies of co-

herence and transfer function versus frequency follow the same broad outlines as for alongshore velocity.

Results for cross-shelf velocity (Figure 8, third row) predict extremely high coherences between currents and winds but low gains ($< 0.75 \text{ cm s}^{-1} (\text{dyn cm}^{-2})^{-1}$). Recall that these predictions are only for the region outside the surface and bottom boundary layers, so that Ekman transports are not included. Wind-onshore current gain R_{uT} increases with increasing frequency (not shown), in contrast to results for alongshore velocity and pressure. The ratio of predicted cross-shelf to alongshore current variance at midshelf for $\omega = 1.08 \times 10^{-5} \text{ s}^{-1}$ is about 0.0068 and increases with increasing frequency. Observations yield numbers typically a factor of 10 higher at the lower frequencies, suggesting that the present model does an inadequate job with cross-shelf currents. This result is not surprising in light of the above discussion of \bar{u} as a function of alongshore wave number.

Predicted density fluctuations (Figure 8, bottom row) over the shelf are highly coherent with alongshore winds and generally lag by $45^\circ\text{--}90^\circ$, with greater lags near the coast. Gains are largest close to the coastal wall and in the upper water column, although they are nearly zero at the surface where the wind stress curl does not exist [because of (1e) and (2b)]. Predicted gains are about a factor of 50 smaller than those observed in the summer of 1982. This gross discrepancy between observations and the model is probably due to a combination of the neglect of frontal and mixed layer physics and to the spectral resolution problem also encountered with the cross-shelf velocity component.

Comparison with observations suggests that density fluctuations and cross-shelf currents are very poorly resolved by the present model. The following discussion will not treat these variables any further. A detailed comparison of model predictions of v and p with observations is deferred to section 6.

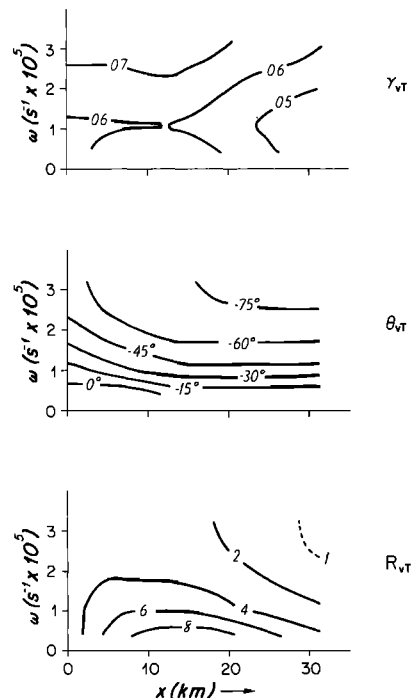


Fig. 9. Response of alongshore velocity v as a function of frequency and distance offshore for the basic case at $z = -50.0$ m. (top) Coherence γ_{vT} , (middle) Phase θ_{vT} , (bottom) Gain R_{vT} . Units are $\text{cm s}^{-1} (\text{dyn cm}^{-2})^{-1}$.

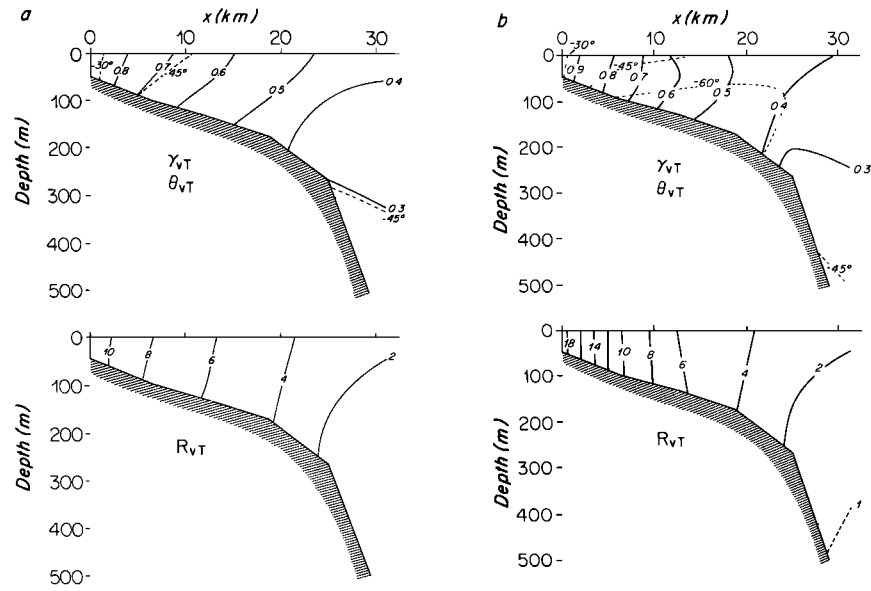


Fig. 10. Response of alongshore velocity v as a function of position at $\omega = 1.08 \times 10^{-5} \text{ s}^{-1}$. Top panels show coherence γ_{vT} (solid contours) and phase θ_{vT} (dotted contours). Bottom panels show gain R_{vT} ($\text{cm s}^{-1} (\text{dyn cm}^{-2})^{-1}$). (a) As in the basic case, but no wind stress curl (long-dashed line in the top panel of Figure 1). (b) As in the basic case, but with intensified winds near the coast (short dashed line in the top panel of Figure 1).

5.2. Wind Stress Curl and Divergence

If the wind stress curl is neglected (equivalent to setting $L_w = 0$ in (11), the response of alongshore velocity (Figure 10a) changes considerably. Maximum coherence and gain occur at the coast instead of at midshelf, and peak values become larger by 30 percent or more. Further, the gain becomes more nearly vertically uniform over the shelf proper. Cross-shelf phase shifts become more pronounced, and the currents everywhere lag winds by a greater amount. The pressure field (not shown) is less strongly affected by the change in wind structure, although its coherence and gain do increase

slightly near the coast. These tendencies become more exaggerated in the case of stronger winds near the coast (Figure 1, top panel, short-dashed line; Figure 10b). In this case, coherences become extremely high nearshore (> 0.9), and gains increase in this area by an amount greater than the proportional increase in local wind stress. Phase lags increase further, and become more depth-dependent. We can safely conclude that the presence of a substantial wind stress curl plays an important role in determining the structure of the current response over the shelf.

Another aspect of the wind field, present in this model but not normally incorporated, is the wind stress divergence. This

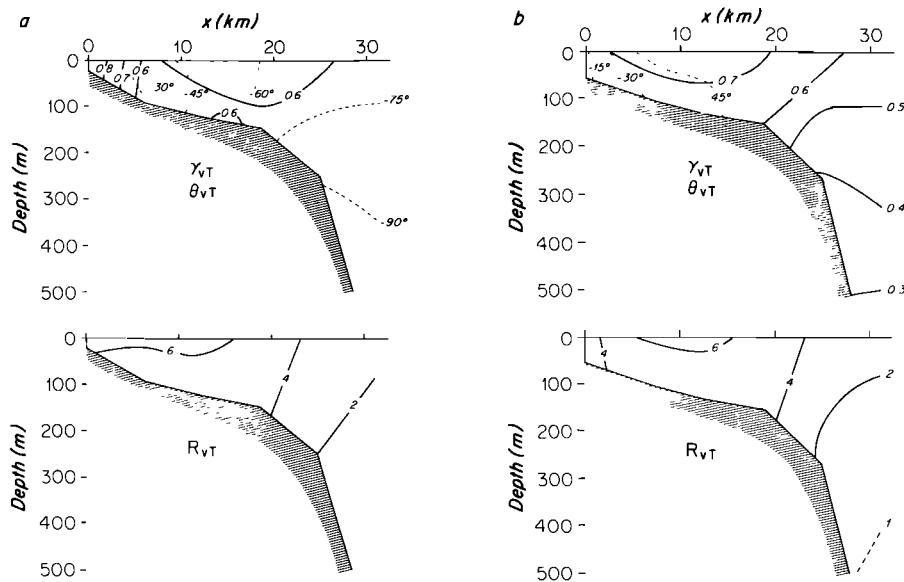


Fig. 11. Variables plotted as in Figure 10. (a) As in the basic case, except no gravity waves, $A_0 = 0.0$ (long-dashed line in the bottom panel of Figure 1). (b) As in the basic case, except $A_0 = 1.0 \text{ m}$ (short-dashed line in the bottom panel of Figure 1).

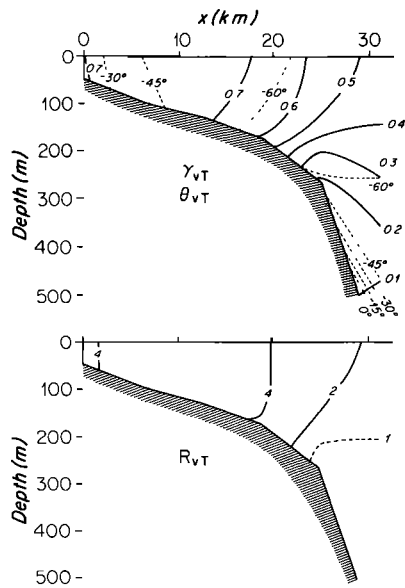


Fig. 12. Variables plotted as in Figure 10, computed for the basic case but with modified stratification (dashed line in the right panel of Figure 1).

effect is represented by the τ_{0y} term in (2b). Since this forcing component is proportional to ωl , it is expected to be most pronounced at high frequencies. A check at $\omega = 3.18 \times 10^{-5} \text{ s}^{-1}$ (2.3-day period, now shown), the highest frequency treated, shows negligible differences in the v response when the divergence is neglected. This insensitivity to divergence carries over to the prediction of u as well.

5.3. Bottom Stress Parameterization

The bottom stress is varied by changing the incident wave height A_0 in the Grant and Madsen [1979] bottom stress formulation (Figure 1). The case of $A_0 = 0$ corresponds to traditional representations of bottom stress, since r is then constant

at 0.0376 cm s^{-1} . The resulting alongshore current response (Figure 11a) differs considerably from the basic case (Figure 8). Coherence and gain increase considerably in relation to the control case (Figure 8) near the coast, and coherence does not decrease as quickly over the shelf. Cross-shelf phase gradients increase considerably and become more monotonic far from the coast. With $A_0 = 0$ and no wind stress curl (not shown), coherence and phase vary extremely rapidly over the inner shelf ($x < 6 \text{ km}$), and peak gains of over $18 \text{ cm s}^{-1} (\text{dyn cm}^{-2})^{-1}$ occur.

With larger surface waves, hence stronger bottom friction (Figure 11b), differences from the control case are less pronounced. Coherence over the shelf increases everywhere by about 0.1, and the cross-shelf phase differences are enhanced so that nearshore currents are almost in phase with the wind stress. The reduction in phase difference is to be expected if the bottom stress plays an enhanced role in balancing the local wind stress. Interestingly, the gain R_{vT} does not change substantially when friction is increased. This seems to reflect the competing tendencies of increased coherence but decreased energy levels.

We conclude that results are rather sensitive to estimates of friction that are relatively small. In contrast, results seem less sensitive to parameter choices in the presence of larger frictional estimates.

5.4. Stratification

The stratification used in the control case is more nearly representative of the region over the slope or far offshore of the upwelling front than over the shelf. The N^2 profile shown by a dashed line in Figure 1 is more representative of that over the shelf, inshore of the upwelling front. When the weaker stratification is used rather than the basic stratification, coherence over the shelf tends to be higher, while that over the slope tends to be lower (Figure 12). Cross-shelf phase gradients are also enhanced. The gain is rather similar, although its value, like that of coherence, tends to be more depth-independent that it is with the basic stratification.

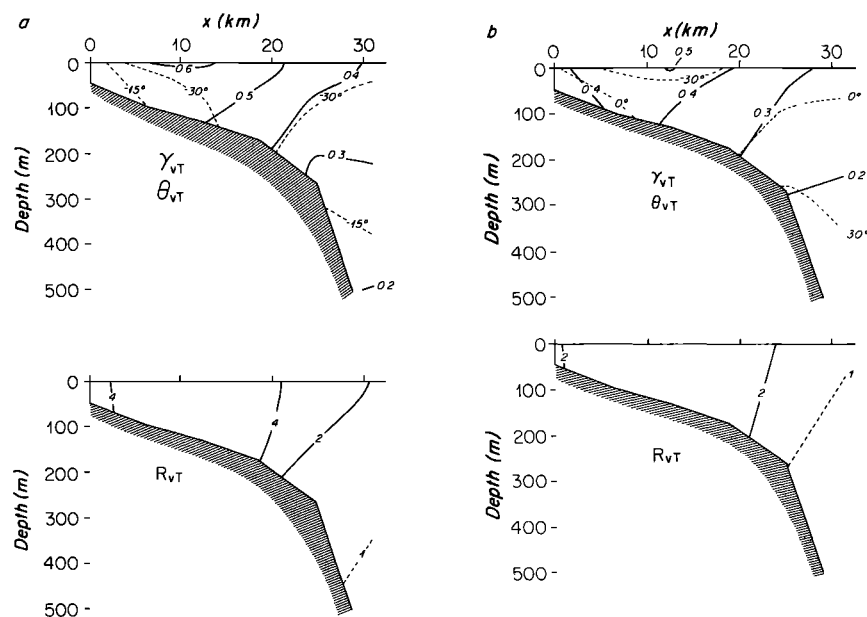


Fig. 13. Variables plotted as in Figure 10, computed (a) for the basic case but with the measured wind stress spectrum and (b) for the basic case but with a white wave number spectrum.

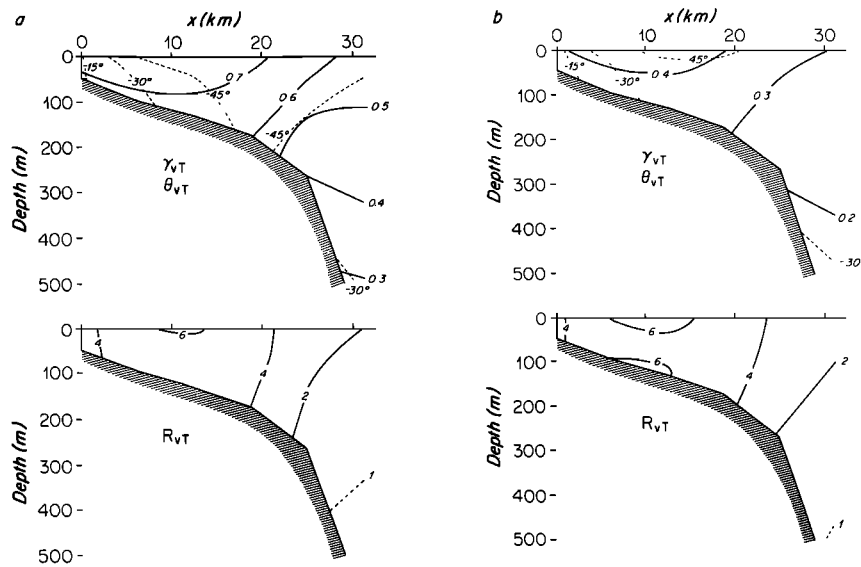


Fig. 14. Variables plotted as in Figure 10, computed for the basic case with (a) $l_1 = 0.25 \times 10^{-8} \text{ cm}^{-1}$ and (b) $l_1 = -0.25 \times 10^{-8}$.

Stronger stratification in the upper ocean appears to allow for greater surface intensification of the response.

5.5. Spectral Shape

Because the response of currents to winds depends critically on wind stress spectral shape through (6) and (7), it is worth exploring sensitivity to these values. First, as a “reasonable” variation on the Bakun wind stress spectrum (Figure 2a), the control case was recomputed with a “mirror image” wind stress spectrum $S_T(-l_R, \omega)$. Results (not shown) are virtually identical for coherence and gain between winds and alongshore currents. The cross-shelf phase gradient is somewhat enhanced, and in some locations, phases changed by as much as 10° relative to the case with $S_T(l_R, \omega)$. The conclusion is that moderate variations in spectral shape do not cause inordinate changes in the response.

Use of the measured wind stress spectrum (Figure 2b) causes a more noticeable change because of its relatively larger energy at high wave numbers. At $\omega = 1.08 \times 10^{-5} \text{ s}^{-1}$ (6.7-day period), both the wind stress-current coherence and gain decrease everywhere by about 10% (Figure 13a). Further, the cross-shelf gradients in phase become intensified, particularly near the shelf break. These effects are apparently associated with the increased excitation of higher-mode coastal-trapped waves relative to the Bakun spectrum. At higher frequencies, where the measured wind stress spectrum becomes even whiter, the decrease in coherence becomes more pronounced (see Figure 18, below).

Changing to a white spectrum of the form

$$S_T(l_R, \omega) = 1.0 \quad |l_R| \leq 1.25 \times 10^{-7} \text{ cm}^{-1}$$

$$S_T(l_R, \omega) = 0 \quad |l_R| > 1.25 \times 10^{-7} \text{ cm}^{-1}$$

causes greater changes (Figure 13b). Coherence and gain both decrease substantially, especially over the shelf. The response is also more nearly in phase with local winds than it is in the previous cases, at least for $x < 25 \text{ km}$. The decreased coherence can again be accounted for by the increased contribution of higher (e.g., second) mode resonances to the cross spectrum (equation 6)).

5.6. Complex Wave Numbers

Up to this point, it has been assumed that the wind stress has equal magnitudes all along the coast. If this assumption is relaxed, we might very well expect different behavior, based on the discussion in section 4.

First, consider a wind stress which grows stronger in the direction of free wave propagation (toward the north off California), $l_1 > 0$. The results for $l_1 = 0.25 \times 10^{-8} \text{ cm}^{-1}$ (Figure 14a) show larger coherence between local winds and currents than with $l_1 = 0$, a result that could be anticipated from the slower phase variations with l_R when $l_1 > 0$ in Figure 7. The gain remains about the same as for uniform wind stress, a result which apparently reflects the competing influences of smaller $|\bar{v}|$ in (7) (leading to less energetic fluctuations) and the increased coherence. Cross-shelf phase gradients are larger than in the uniform wind case, and the phase gradient changes

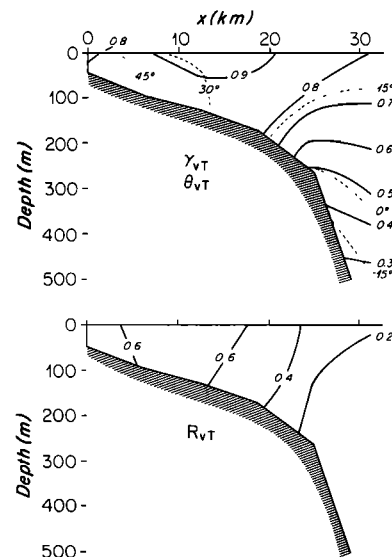


Fig. 15. Variables plotted as in Figure 10, computed for the basic case, but with cross-shelf wind driving.

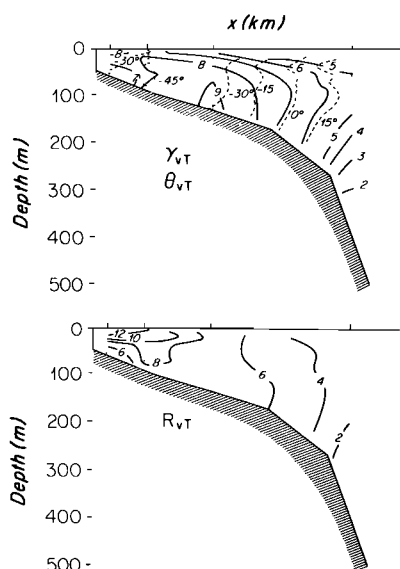


Fig. 16. Observed coherence γ_{vT} , phase θ_{vT} , and gain R_{vT} for CODE 2 for $\omega = 1.08 \times 10^{-5} \text{ s}^{-1}$, plotted as in Figure 10.

sign on the outer shelf. This latter tendency also exists for $l_t = 0$, but it is less pronounced. The reversal in phase tendency is a reflection of the spatial variation of the relative importance of the first and second coastal-trapped wave modes as a function of (x, z) position. The second mode has a node in the area $x > 25 \text{ km}$, $-250 \text{ m} < z < 0$, and the first-mode response is more nearly in phase with the wind for these parameters.

When winds decrease in the direction of coastal-trapped wave propagation (toward the north off California), the transfer function \bar{v} passes close to the complex "resonance" with the damped first-mode coastal-trapped wave (Figure 7). The consequent high values for $|\bar{v}|$ and rapid phase variations lead to a response (Figure 14b) which is more energetic and less coherent than is the case for uniform wind amplitudes. These tendencies again compensate for each other, resulting in a local wind-current gain R_{vT} which is nearly the same as that for $l_t = 0$.

In conclusion, alongshore variations in wind amplitude ($l_t \neq 0$) lead to substantial changes in coherence γ_{vT} . Variation in wind-current phases also occurs, but the variations are not as clearly systematic as those for the other diagnostics.

5.7. Cross-Shelf Wind Stress

The cross-shelf component of wind stress is typically considered to be relatively ineffective for driving alongshore currents [e.g., Csanady 1982; Mitchum and Clarke, 1986b]. Indeed, in the long-wave limit, this can be readily shown by scaling arguments. This issue can be explored for a general parameter range with the present model. One difficulty, however, is that a reliable wave number-frequency spectrum for cross-shelf wind stress is not available. To circumvent this point, the alongshore and cross-shelf wind stress are assumed to have the same spectral shapes (although not levels) and cross-shelf structure.

The results demonstrate that at $\omega = 1.08 \times 10^{-5} \text{ s}^{-1}$ (6.7-day period), the cross-shelf wind stress is indeed ineffectual for driving alongshore currents (Figure 15). This result (on a per dyne per square centimeter basis) is compounded by the fact that in most locations, cross-shelf winds are much weaker

than alongshore winds. Cross-shelf current u gains with τ_0^x are also smaller than those for τ_0^y at this frequency, but only by about a factor of 5. At higher frequencies ($\omega = 3.18 \times 10^{-5} \text{ s}^{-1}$ or 2.3-day period), cross-shelf wind stress becomes potentially more important. In this case, gains R_{vT} are only about a factor of 2 smaller for τ_0^x , and R_{uT} is about the same magnitude for both τ_0^x and τ_0^y .

We conclude that for frequencies comparable to the inertial, cross-shelf wind stress can be an effective driving agency. Whether such a response could be observed depends on the cross-shelf wind stress being at least comparable in magnitude to the alongshelf wind stress and on the two stress components themselves being statistically distinguishable.

6. COMPARISON WITH OBSERVATIONS

The model coherences, phases, and gains described in section 5 can be compared with observations obtained along the CODE central line ($\sim 38^\circ 30' \text{N}$) during CODE 2 (April 13, 1982 to July 25, 1982). The details of the mooring locations, instrumentation, and data return are described by Limeburner [1985]. A total of 29 current meters were distributed among four moorings along the central line. The moorings, designated C2, C3, C4, and C5, were deployed in total water depths of 60, 90, 130, and 400 m, respectively. The mooring locations are shown in Figure 1. Bottom pressure records were obtained at C2, C3, and C4. Wind speed and direction measured at a surface buoy at C3 were chosen to represent the midshelf wind field. Wind stress was estimated using the method of Large and Pond [1981]. The coherence, phase, and gain of the alongshore (317°T) component of wind stress with temperature and velocity components from each current meter as well as with each bottom pressure record were computed (using the unfiltered, hourly averaged time series) at frequency bands centered on the frequencies used in the model ($\omega = 0.38, 1.08, 1.78, 2.48, \text{ and } 3.18 \times 10^{-5} \text{ s}^{-1}$). Each cross-spectral estimate has 20 degrees of freedom. The cross-shelf wind stress was not considered, as it is much weaker than the alongshore component, hence presumably unimportant.

The observed cross-shelf structure of coherence, phase, and gain for alongshore velocity at $\omega = 1.08 \times 10^{-5} \text{ s}^{-1}$ is shown in Figure 16 (compare Figure 8). The coherence is significant at 95% confidence ($\gamma > 0.53$) throughout the entire water column at C2, C3, and C4, reaching a maximum near the bottom at C4. The coherence decreases rapidly toward the shelf break. The phase changes by about 50° , with the near-shore currents leading those offshore until near the shelf break (negative phase means that the wind leads the currents). The near-surface gain is largest nearshore and decreases rapidly in the offshore direction. At 50-m depth, the maximum gain occurs at midshelf. Each plot has some qualitative features similar to the model results of Figure 8. However, the quantitative agreement of the detailed structures is generally poor.

Figure 17 shows the observed coherence, phase, and gain for all available frequencies and offshore locations at a depth of 55 m (compare Figure 9). The coherence is highest at midshelf (C3) for all frequencies. Almost all currents (at 55-m depth) are significantly coherent with the wind stress for $\omega < 2 \times 10^{-5} \text{ s}^{-1}$. The coherence decreases to a minimum at $\omega \approx 2.5 \times 10^{-5} \text{ s}^{-1}$ before increasing again at higher frequencies. The phase shows little structure at low frequencies (although nearshore currents lead those farther offshore over the inner 5–15 km), but rapid cross-shelf phase changes occur over the outer shelf at frequencies higher than $\omega \approx 10^{-5} \text{ s}^{-1}$, so that

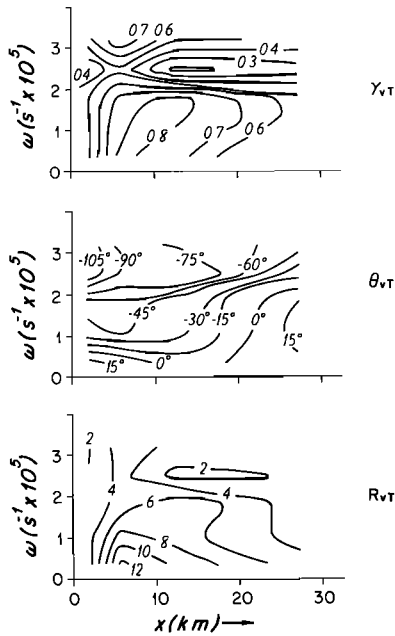


Fig. 17. Response of observed alongshore currents v to alongshore wind stress as a function of cross-shelf distance and frequency at $z = -55$ m, plotted as in Figure 9.

the midshelf motions lag those over the slope. The gain is largest at low frequencies and midshelf locations and decreases rapidly with increasing frequency. Again, the quantitative agreement with the model results of Figure 9 appears poor, although some qualitative agreement can be seen.

A direct comparison of model and observed quantities is presented in Figure 18, where coherence, phase, and gain are plotted versus frequency for selected records. The solid line connects observed values, while the solid dots are the model predictions for the basic example (Bakun wind stress spectrum) of section 5.1. The open dots are the predictions for the basic example, but with the measured wind stress spectrum.

The crosses will be discussed below. The left panels compare results for bottom pressure at C2, while the middle and right panels compare velocity results from C3 (70 m) and C4 (90 m), respectively. The comparisons are similar in all cases. At low frequencies the observed coherence is higher than the model coherence using the Bakun spectrum, but agreement improves at the two highest frequencies. The model coherences using the measured spectrum are similar to those using the Bakun wind stress spectrum at low frequencies, but they are considerably lower at high frequencies. In contrast to the model results using the Bakun spectrum (which increases with frequency), the model results using the measured spectrum do not have noticeably increased coherence at higher frequencies (they have only a minuscule rise in coherence at about $2.6 \times 10^{-5} \text{ s}^{-1}$ and then a decrease at $3.10 \times 10^{-5} \text{ s}^{-1}$). These differences can all be traced to the whiteness of the measured wind stress spectrum and the consequent tendency to excite free coastally-trapped waves. All phase estimates are quite similar (decreasing with increasing frequency), and the model predictions are often within the 95% error bounds (vertical lines) of the observed phase. The gains for both models tend to be lower than the observed gains, but they show the same tendency to decrease with increasing frequency.

Overall, there are substantial differences between the observations and the model predictions for the basic example of section 5.1. However, the reader should keep in mind that the model has not been tuned to fit the observations. In fact, there is little reason to believe that the basic example is necessarily the most realistic.

7. AN "OPTIMAL" MODEL

Up to this point, model inputs have been chosen with the object of being representative but not necessarily accurate. This section now presents the results of the model using the most realistic (based on data) choice of parameters. The inputs are nearly the same as those for our basic case, but with three exceptions. First, the reduced "shelf" stratification (dashed line in the right panel of Figure 1, also used for Figure 12) is used.

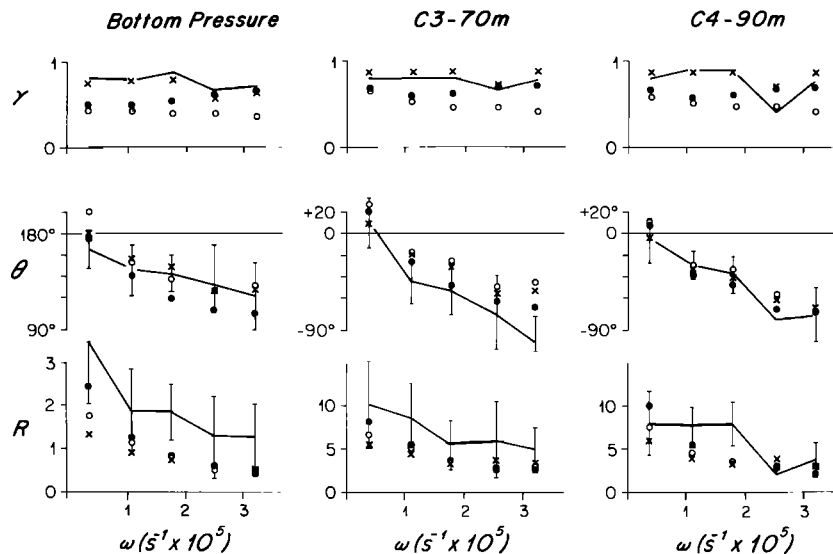


Fig. 18. Response of current and pressure to winds. Basic model results are shown by dots (solid, Bakun wind stress spectrum; open, measured wind stress spectrum), and optimal model results are shown by crosses. Observed results are connected by solid lines, and 95% confidence limits are given (where coherence is significant) for phase and transfer function. The left column shows bottom pressure at C2 (transfer function in $\text{mbar} (\text{dyn cm}^{-2})^{-1}$). The middle column shows alongshore velocity at C3 at 70-m depth (transfer function in $\text{cm s}^{-1} (\text{dyn cm}^{-2})^{-1}$). The right column shows alongshore velocity at C4 at 90-m depth. Top row, coherence; middle row, phase; bottom row, gain.

TABLE 1. Estimates of Imaginary Wave Number, April–July 1982

Frequency, $s^{-1} \times 10^5$	G	l_i $cm^{-1} \times 10^8$
0.38	0.256	1.50
1.08	0.203	1.75
1.78	0.170	1.94
2.48	0.725	0.35
3.18	0.192	1.81

Second, the measured wind stress spectrum is used, rather than the Bakun wind stress spectrum, although results in this case are nearly identical with either spectrum. Third, and most importantly, alongshore variations in the amplitude of the wind stress, $l_i \neq 0$, are included. Effectively, the spectral levels are assumed to increase exponentially northward along the California coast between Point Conception ($34^\circ 30'N$) and the CODE area ($38^\circ 30'N$). The spectral levels for wind stress at NDBO buoys 46013 (CODE area) and 46011 at each frequency were then compared in order to estimate the l_i values shown in Table 1. Also shown in this table is the ratio

$$G = \frac{\text{spectral density (46011)}}{\text{spectral density (46013)}}$$

to dramatize the differences in wind variability over the 455-km separation. For all five frequencies, CODE winds are stronger ($l_i > 0$), although for $\omega = 2.48 \times 10^{-5} s^{-1}$ (2.9-day period), they are only slightly stronger ($G = 0.725$).

The results of these calculations are shown in various ways in Figures 18, 19, and 20. First, for comparison with earlier calculations, consider the plots of alongshore velocity response at $\omega = 1.08 \times 10^{-5} s^{-1}$ (6.7-day period) (Figure 19). The strong tendency for winds to increase towards the north, $l_i = 1.75 \times 10^{-8} cm^{-1}$, leads to very high wind-current coherences (> 0.8) over the central shelf. Also, compared to Figure 12 or 13a ($l_i = 0.0$), the phase tends more rapidly toward positive

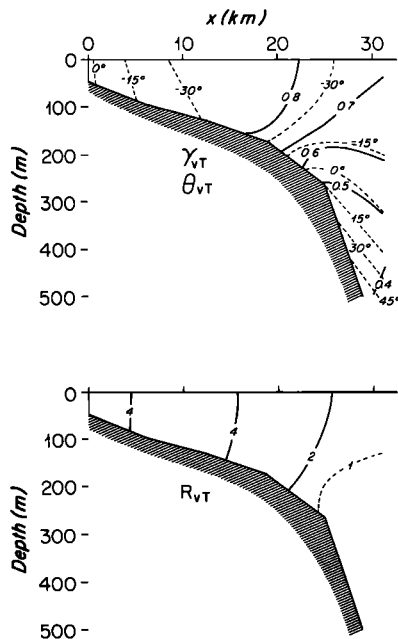


Fig. 19. Response of alongshore currents to wind stress at $\omega = 1.08 \times 10^{-5} s^{-1}$ as a function of position for the optimal model, plotted as in Figure 10.

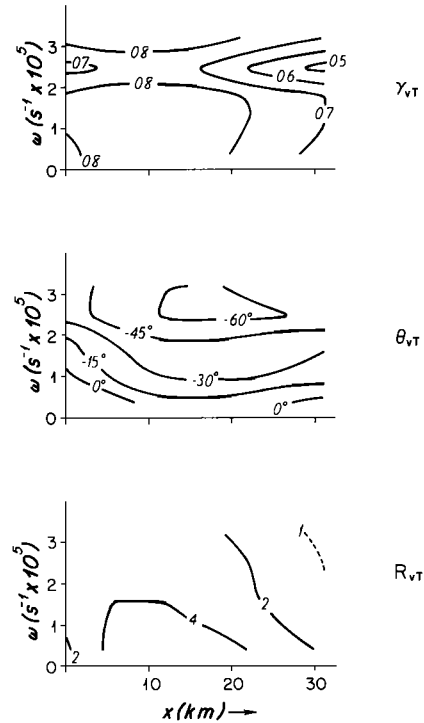


Fig. 20. Response of alongshore currents to wind stress for the optimal model at 50-m depth, plotted as in Figure 9.

values near the shelf break. These aspects both represent improvements over the basic case of section 5.

The response as a function of frequency (crosses in Figure 18) also shows a general improvement compared with the basic case. Coherences are now closer to their observed high values, and more interestingly, the dip in coherence at $\omega = 2.48 \times 10^{-5} s^{-1}$ is now qualitatively reproduced. Phases and gains for these three observables (bottom pressure at C2 and alongshore velocity at C3 (70 m) and C4 (90 m)) are reproduced about as well as before. Response of alongshore velocity at 50 m as a function of frequency and x (Figure 20) again shows some tendency to duplicate observed patterns (Figure 17), especially the coherence dip near $\omega = 2.48 \times 10^{-5} s^{-1}$. The qualitative patterns in gain are also duplicated fairly well. Phases agree generally for $\omega \lesssim 1.2 \times 10^{-5} s^{-1}$ and $x < 15$ km. The observed phase estimates from $x = 27.25$ km (C4) and near $\omega = 2.48 \times 10^{-5} s^{-1}$ are generally accompanied by very low coherences and hence have large error bounds (in the range of $\pm 25^\circ$ to $> 60^\circ$ at 95% confidence). Thus we expect that at least some of the phase disagreements are a result of poor estimates from data. Nonetheless, at least some of the qualitative tendencies in the data are reproduced by the model, such as the general decrease in phase with increasing frequency.

A similar "optimal" calculation was also attempted for the winter of 1981–1982. Since no small-scale array of wind measurement was in place, the wind was allowed to vary in the cross-shelf direction in the same way as for the summer of 1982. Estimates of the l_i were again made using data from the CODE and Point Conception areas, leading to estimates typically twice those in summer 1982. A 1981–1982 wintertime Bakun wind stress spectrum was also used for the real part of the wave number. (The Bakun and measured spectra are nearly identical for this period.) The results (not shown) were something of a disappointment, as model coherences were

typically higher than observed coherences by 0.3 over the shelf. A likely cause for failure may lie in the assumption that wind stress amplitude increased monotonically up to the CODE area, allowing parameterization in terms of a complex wave number. Chapman [this issue] has shown that the winds during this period were apparently of similar strength for about 100–200 km south of the CODE area and then decreased quickly toward the south. Such a distribution of wind stress amplitude could well result in lower observed coherences than those estimated with our winter model.

8. CONCLUSIONS

The use of a stochastic model to predict the wind response of oceanographic variables can provide some illumination of observed results. For example, the study of frequency-wave number transfer functions and wind stress spectra leads to some simple conclusions about the importance of free coastal-trapped waves. At low frequencies (20-day period in this case), these waves are not very evident because of frictional damping. At high frequencies ($\omega = 3.18 \times 10^{-5} \text{ s}^{-1}$) the waves are not noticeably excited if the wave number spectrum of wind stress is red enough, because there is little wind stress energy at the “resonant” space and time scales. These waves are more (less) important at midfrequencies if the wind stress decreases (increases) in the direction of free-wave propagation. Such conclusions could, of course, be also reached by other lines of reasoning [e.g., Allen, 1976]. Perhaps more interestingly, the results suggest that accurate prediction of temperature and cross-shelf current fluctuations outside turbulent boundary layers usually are not possible given the quality of inputs available. The situation is especially discouraging for cross-shelf velocity, where the transfer function \bar{u} increases monotonically (Figure 6) out to alongshore wavelengths as short as 60 km. In this context it is interesting to note the unusual circumstances off Peru near 15°S, where in the interior, significant u - τ^y correlations were observed but significant v - τ^y correlations were not observed [Brink et al., 1980]. The alongshore wind stress was dominated by very short alongshore wavelengths, of the order of 50–60 km [Stuart and Moody, 1981]. This scale of wind stress fluctuations complements the properties of the \bar{u} transfer functions, but not the \bar{v} , and thus appears to rationalize the observations.

To the extent that model results duplicate observed phenomena, we can conclude what inputs are important for predicting pressure and alongshore current fluctuations over the shelf. The model results tend to overpredict wind-current coherence in the upper 20–50 m of the water column. This may be attributed, at least partially, to the neglect of mixed layer and frontal physics. Fronts, for example, could lead to loss of coherence if they move in a manner which is not related to the wind in the same way as the linearized model interior or if they become unstable, resulting in superficial eddies. Neglect of upper ocean processes also undoubtedly detracts from the model's ability to predict density variations. Perhaps a more disturbing failure of this model, as well as of some first-order wave equation models [e.g., Mitchum and Clarke, 1986a; Chapman, this issue], is that the model systematically underpredicts the gains for current fluctuations. It is not obvious why this problem should occur, but the present gain results do suggest that it is not simply because wind stresses are consistently underestimated from observations. Rather, it seems that the stochastic and coastal-trapped wave models somehow un-

derpredict the actual wind-current coupling because of some other, still unknown, effect.

In some regards the model did perform well, at least qualitatively, so that some conclusions can be drawn. The ability of the model to predict correctly maximum wind-current coherence at midshelf depended on the inclusion of a realistic cross-shelf wind stress gradient. The model's skill at obtaining coherences as high as those observed at C4 and its tendency to reproduce the coherence dip at $\omega = 2.48 \times 10^{-5} \text{ cm}^{-1}$ both depend on the inclusion of a complex wave number. Thus at least for the California coast, alongshore gradients in wind amplitude are demonstrably important. When complex wave numbers are allowed, results become less sensitive to the details of real wave number wind stress spectra. Finally, the neglect of a Grant and Madsen [1979] type bottom boundary layer parameterization [Figure 11a] led to serious difficulties with coherence, phase, and gain structures. The comparison with “observables” confirms the supposition of Clarke and Brink [1985] that the form of bottom friction is important. It thus seems clear that some accounting for wave-current interaction must be made in a successful model.

Acknowledgments. We thank the investigators of the CODE program for making their data and results freely available to us. This work was supported by National Science Foundation grant OCE84-08563.

REFERENCES

- Allen, J. S., Some aspects of the forced wave response of stratified coastal regions, *J. Phys. Oceanogr.*, **6**, 113–119, 1976.
- Allen, J. S., and D. W. Denbo, Statistical characteristics of the large-scale response of coastal sea level to atmospheric forcing, *J. Phys. Oceanogr.*, **14**, 1079–1094, 1984.
- Bakun, A., Coastal upwelling indices, west coast of North America, 1946–71, *NOAA Tech. Rep., NMFS SSRF 671*, 103 pp., 1973.
- Battisti, D. S., and B. M. Hickey, Application of remote wind-forced coastal trapped wave theory to the Oregon and Washington coasts, *J. Phys. Oceanogr.*, **14**, 887–903, 1984.
- Beardsley, R. C., C. E. Dorman, C. A. Friehe, L. K. Rosenfeld, and C. D. Winant, Local atmospheric forcing during the Coastal Ocean Dynamics Experiment, I, A description of the marine boundary layer and atmospheric conditions over a northern California upwelling region, *J. Geophys. Res.*, this issue.
- Brink, K. H., Propagation of barotropic continental shelf waves over irregular bottom topography, *J. Phys. Oceanogr.*, **10**, 765–778, 1980.
- Brink, K. H., A comparison of long coastal trapped wave theory with observations off Peru, *J. Phys. Oceanogr.*, **12**, 897–913, 1982.
- Brink, K. H., and J. S. Allen, Reply, *J. Phys. Oceanogr.*, **13**(1), 149–150, 1983.
- Brink, K. H., and D. C. Chapman, Programs for computing properties of coastal-trapped waves and wind-driven motions over the continental shelf and slope, *Tech. Rep. 85-17*, 98 pp., Woods Hole Oceanogr. Inst., Woods Hole, Mass., 1985.
- Brink, K. H., D. Halpern, and R. L. Smith, Circulation in the Peruvian upwelling system near 15°S, *J. Geophys. Res.*, **85**, 4036–4048, 1980.
- Chapman, D. C., Application of wind-forced long, coastal-trapped wave theory along the California coast, *J. Geophys. Res.*, this issue.
- Clarke, A. J., and K. H. Brink, The response of stratified, frictional flow of shelf and slope waters to fluctuating large-scale low-frequency wind forcing, *J. Phys. Oceanogr.*, **15**, 439–453, 1985.
- Csanady, G. T., *Circulation in the Coastal Ocean*, 279 pp., D. Reidel, Hingham, Mass., 1982.
- Denbo, D. W., and J. S. Allen, Large-scale response to atmospheric forcing of shelf currents and coastal sea level off the west coast of North America: May–July 1981 and 1982, *J. Geophys. Res.*, this issue.
- Gill, A. E., and E. H. Schumann, The generation of long shelf waves by the wind, *J. Phys. Oceanogr.*, **4**, 83–90, 1974.
- Grant, W. D., and O. S. Madsen, Combined wave and current interaction with a rough bottom, *J. Geophys. Res.*, **84**, 1797–1808, 1979.

- Halliwell, G. R., Jr., and J. S. Allen, The large-scale coastal wind field along the west coast of North America, 1981–1982. *J. Geophys. Res.*, this issue.
- Large, W. G., and S. Pond, Open ocean momentum flux measurements in moderate to strong winds, *J. Phys. Oceanogr.*, *11*, 324–336, 1981.
- Limeburner, R. (Ed.), CODE-2: Moored array and large-scale data report, *Tech. Rep. 85-35*, 233 pp., Woods Hole Oceanogr. Inst., Woods Hole, Mass., 1985.
- Mitchum, G. T., and A. J. Clarke, Evaluation of frictional, wind forced long wave theory on the west Florida Shelf, *J. Phys. Oceanogr.*, *16*, 1029–1037, 1986a.
- Mitchum, G. T., and A. J. Clarke, The frictional nearshore response to forcing by synoptic scale winds, *J. Phys. Oceanogr.*, *16*, 934–946, 1986b.
- Müller, P., and C. Frankignoul, Direct atmospheric forcing of geostrophic eddies, *J. Phys. Oceanogr.*, *11*, 287–308, 1981.
- Spillane, M. C., A model of wind-forced viscous circulation near coastal boundaries, Ph.D. thesis, 88 pp., Oreg. State Univ., Corvallis, 1980.
- Stuart, D. W., and G. L. Moody, Atlas of the JOINT II 1977 aircraft winds for the 500 foot level, *CUEA Tech. Rept. 66*, 63 pp., Fla. State Univ., Tallahassee, 1981.
- Winant, C. D., R. C. Beardsley, and R. E. Davis, Moored wind, temperature, and current observations made during Coastal Ocean Dynamics Experiments 1 and 2 over the northern California continental shelf and upper slope, *J. Geophys. Res.*, this issue.
- Wright, D. G., and K. R. Thompson, Time-averaged forms of the non-linear stress law, *J. Phys. Oceanogr.*, *13*, 341–345, 1983.
-
- K. H. Brink and D. C. Chapman, Woods Hole Oceanographic Institution, Woods Hole, MA 02543.
- G. R. Halliwell, Jr., Graduate School of Oceanography, University of Rhode Island, Narragansett, RI 02882.

(Received July 31, 1986;
accepted September 9, 1986.)